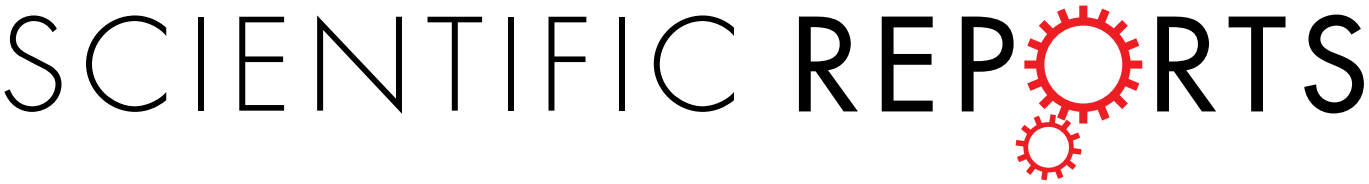

OPEN

Electronic Structure Evolution with Composition Alteration of Rh_xCu_y Alloy Nanoparticles

Received: 23 June 2016
Accepted: 19 December 2016
Published: 25 January 2017

Natalia Palina[1], Osami Sakata[1,2,3], L. S. R. Kumara[1], Chulho Song[1], Katsutoshi Sato[4,5], Katsutoshi Nagaoka[5], Tokutaro Komatsu[6], Hirokazu Kobayashi[7], Kohei Kusada[7] & Hiroshi Kitagawa[7,8,9]

The change in electronic structure of extremely small Rh_xCu_y alloy nanoparticles (NPs) with composition variation was investigated by core-level (CL) and valence-band (VB) hard X-ray photoelectron spectroscopy. A combination of CL and VB spectra analyses confirmed that intermetallic charge transfer occurs between Rh and Cu. This is an important compensation mechanism that helps to explain the relationship between the catalytic activity and composition of Rh_xCu_y alloy NPs. For monometallic Rh and Rh-rich alloy ($Rh_{0.77}Cu_{0.23}$) NPs, the formation of Rh surface oxide with a non-integer oxidation state ($Rh^{(3-\delta)+}$) resulted in high catalytic activity. Conversely, for alloy NPs with comparable Rh:Cu ratio ($Rh_{0.53}Cu_{0.47}$ and $Rh_{0.50}Cu_{0.50}$), the decreased fraction of catalytically active $Rh^{(3-\delta)+}$ oxide is compensated by charge transfer from Cu to Rh. As a result, ensuring negligible change in the catalytic activities of the NPs with comparable Rh:Cu ratio to those of Rh-rich and monometallic Rh NPs.

Interest in alloy catalysts is driven by initial industry demand for bimetallic catalysts[1–3] and quantum theory of alloys; in particular, theories predicting the surface composition of alloys[4,5]. Compared with their monometallic components, bimetallic systems are also expected to display unique properties that are not characteristic of the monometallic constituents because of a possible synergistic effect between the two metals. Most catalytically active metals are transition metals with frontier d-orbitals, so considerable effort has been dedicated to d-band modification. Hammer and Nørskov developed the d-band center model, which correlates electronic structure to catalyst reactivity[6,7]. This model introduces the following ideas: alloying causes (i) narrowing of the d-band, which is the main change, and either (ii) electron transfer to one alloy component or (iii) certain rehybridisation of all alloy components. The d-band center model readily explains some experimental data[8–11]. It is believed that the narrowing of d-band width is a general trend in alloys. To avoid confusion, we should stress that changes in electronic structure that are caused by post-fabrication modifications such as exposure to reactive gases, annealing or other intentional surface modification can possibly lead to broadening of the d-band width and are not considered here.

With the rapid growth of the number of automobiles in the modern world, effective three-way catalysts (TWCs) to purify harmful exhaust gases including nitrogen oxides (NOx), carbon monoxide (CO) and hydrocarbons have increasingly been viewed as a necessary technology to prevent serious atmospheric pollution[12–15]. As their name reflects, TWCs are used for the simultaneous and effective treatment of the major pollutants

[1]Synchrotron X-ray Station at SPring-8, Research Network and Facility Services Division, National Institute for Materials Science (NIMS), 1-1-1 Kouto, Sayo-cho, Sayo-gun, Hyogo 679-5148, Japan. [2]Synchrotron X-ray Group, Research Center for Advanced Measurement and Characterization, NIMS, 1-1-1 Kouto, Sayo-cho, Sayo-gun, Hyogo 679-5148, Japan. [3]Department of Materials Science and Engineering, School of Materials and Chemical Technology, Tokyo Institute of Technology, 4259-J3-16, Nagatsuta, Midori, Yokohama 226-8502, Japan. [4]Elements Strategy Initiative for Catalysts and Batteries, Kyoto University, 1-30 Goryo-Ohara, Nishikyo-ku, Kyoto 615-8245, Japan. [5]Department of Applied Chemistry, Faculty of Engineering, Oita University, 700 Dannoharu, Oita 870-1192, Japan. [6]School of Medicine, Nihon University, 30-1, Oyaguchi Kami-cho, Itabashi-ku, Tokyo 173-8610, Japan. [7]Division of Chemistry, Graduate School of Science, Kyoto University, Kitashirakawa Oiwake-cho, Sakyo-ku, Kyoto 606-8502, Japan. [8]Institute for Integrated Cell-Material Sciences (iCeMS), Kyoto University, Yoshida, Sakyo-ku, Kyoto 606-8501, Japan. [9]INAMORI Frontier Research Center, Kyushu University, 744 Motooka, Nishi-ku, Fukuoka 819-0395, Japan. Correspondence and requests for materials should be addressed to N.P. (email: MUELLER.Natalia@nims.go.jp) or O.S. (email: SAKATA.Osami@nims.go.jp)

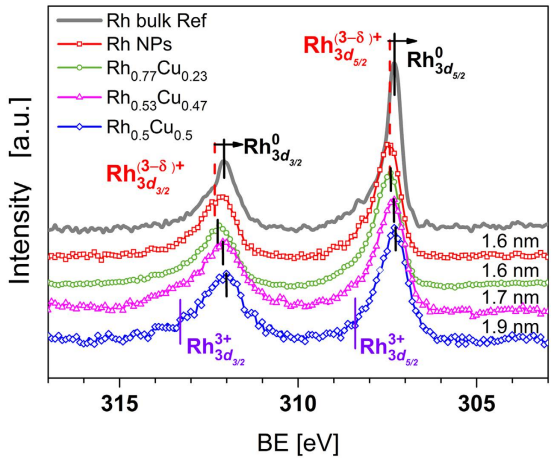

Figure 1. Rh 3*d* CL HAXPES data for reference Rh (solid line), monometallic Rh NPs (red square scatters), $Rh_{0.77}Cu_{0.23}$ (green circle scatters), $Rh_{0.53}Cu_{0.47}$ (magenta triangle scatters) and $Rh_{0.50}Cu_{0.50}$ (blue diamond scatters) alloy NPs. The main peak position of monometallic Rh NPs is shifted towards higher BE compared with that of the reference sample, indicating partial oxidation. With increasing Cu content of the bimetallic alloy NPs, the main peak position recovers to that of Rh^0, indicating intermetallic charge transfer from Cu to Rh in the alloy NPs. The main peak positions for Rh reference are consistent with the Rh^0 BE reported elsewhere[23–26].

stimulated by catalysts. When the reaction conditions are nearing theoretical air-to-fuel ratio, harmful pollutants can be effectively converted to their harmless stable products: carbon dioxide (CO_2), water (H_2O) and nitrogen (N_2). TWCs typically consist of (i) a stainless steel-based monolithic substrate with a honeycomb structure, (ii) a support with high surface area and oxygen storage materials coated on the monolith, (iii) noble metals (Pt, Pd and Rh) as the active catalysts, and (iv) metal oxides that mainly function as promoters[16,17]. Rhodium (Rh) is an indispensable component of TWCs because of its high catalytic activity for NOx reduction[18] and partial oxidation of higher hydrocarbons[19]. However, Rh is one of the most expensive metals because of its scarcity. Therefore, much research has focused on removing the need for excessive use of Rh. This has triggered efforts to synthesise cost-effective, highly stable materials that exhibit catalytic activity comparable with that of noble metals. Alloys of Rh with Cu are candidates for effective TWCs based on the concepts of density of states (DOS) engineering and non-equilibrium synthesis[20–22].

To identify alloy compositions suitable for use as TWCs, here we study the evolution of electronic structure as a function of compositional alteration utilizing hard X-ray photoelectron spectroscopy (HAXPES). Alloy nanoparticles (NPs) are prepared by solid solution synthesis and covered with polyvinylpyrrolidone (PVP) to prevent NPs from agglomeration. The ratio of PVP to the overall metallic content can be estimated as large as 20%, resulting in a PVP protective layer with a thickness of a few nm. This thickness of PVP and its insulating nature make it impossible to utilise laboratory X-ray photoelectron spectroscopy (XPS) tools. In contrast, use of hard X-rays can effectively overcome the above-stated limitation of laboratory XPS instruments and provide reliable data about the electronic states of the metals in the alloy NPs. Information that can be obtained from core level (CL) and valence band (VB) data will help determine the optimal composition of alloys to achieve the most stable and catalytically effective NPs. Note that the Rh_xCu_y NPs investigated in this work exhibit comparable catalytic activity (Supplementary Figure SI 2). Experimentally obtained electronic structure data provide essential inputs for theoretical calculation of realistic alloy NP models, including orbital projected DOS. Such models will aid overall understanding and help to classify the phenomena responsible for electronic structure modification during alloying. The ultimate goals are to control and predict the physicochemical properties of new alloy NPs.

Results and Discussion

CL HAXPES. HAXPES measurements were performed to identify changes in the electronic structure of mono- and bimetallic NPs with different compositions formed by solid solution synthesis. Figures 1 and 2 show the Rh 3*d* and Cu $2p_{3/2}$ CL HAXPES spectra, respectively, of investigated samples along with those of reference bulk metals. The binding energies (BEs) of Rh 3*d* and Cu $2p_{3/2}$ for mono- and bimetallic alloy NPs and reference metals are summarised in Table 1. The peak positions and their assignments are consistent with reported data[23–29]. It should be mentioned that, within the standard deviation of transmission electron microscopy (TEM) results (refer to Supplementary Figure SI 1), the size of NPs discussed here can be regarded as similar. Therefore, the discussion is conducted in terms of evaluation of electronic structure modification with compositional alteration of the alloy excluding size effects.

The change in the electronic structure observed as a result of alloying of Rh and Cu can be understood as concurrent reduction of Rh and oxidation of Cu. Figures 1 and 2 reveal that the CL peaks for Rh 3*d* and Cu $2p_{3/2}$ move in opposite directions, indicating the presence of an intermetallic interaction, which can be viewed as charge transfer from Cu to Rh. This observation is consistent with the Miedema model of metals and alloys, where charge transfer is related to the electronegativity of constituents and typically occurs from atoms of lower to atoms of higher electronegativity[30]. Thus, intuitively for Rh_xCu_y alloy, intermetallic charge transfer is expected to

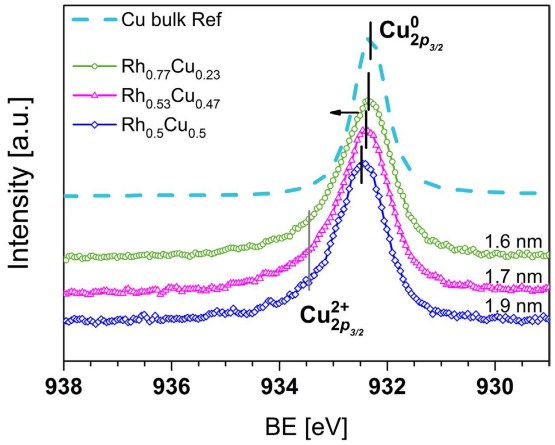

Figure 2. Cu $2p_{3/2}$ CL HAXPES data for reference Cu (dashed line), and $Rh_{0.77}Cu_{0.23}$ (green circle scatters), $Rh_{0.53}Cu_{0.47}$ (magenta triangle scatters) and $Rh_{0.50}Cu_{0.50}$ (blue diamond scatters) alloy NPs. The main peak position of all alloy NPs shifted towards higher BE compared with that of the reference sample, indicating size-dependent partial oxidation of Cu. The main peak positions for the reference are consistent with those reported for metallic Cu[27–29].

Sample	Rh^0 $3d_{5/2}$	$Rh^{(3-\delta)+}$ $3d_{5/2}$	Rh^0 $3d_{3/2}$	$Rh^{(3-\delta)+}$ $3d_{3/2}$	Cu^0 $2p_{3/2}$	Cu^{2+} $2p_{3/2}$
Rh bulk	307.3	—	312.00	—	—	—
Rh NPs	—	307.45	—	312.26	—	—
$Rh_{0.77}Cu_{0.23}$	—	307.43	—	312.25	932.34	933.40
$Rh_{0.53}Cu_{0.47}$	307.32	—	311.97	—	932.37	933.38
$Rh_{0.50}Cu_{0.50}$	307.30	—	311.90	—	932.45	933.40
Cu bulk	—	—	—	—	932.33	933.51

Table 1. Summary of binding energies (BE) of Rh 3*d* and Cu $2p_{3/2}$ representing position of the peak with dominant spectral weight text.

occur from Cu to Rh because the electronegativity values for Cu and Rh are 1.90 and 2.28 according to the Pauling scale, respectively[31]. Even though, the Miedema semi-empirical theory can not predict all features of an alloy, it is applicable to the description of investigated samples. The assumption of charge transfer is further supported by the CL HAXPES data presented here. In particular, with decreasing Rh content, the Rh 3*d* BEs of the bimetallic alloy NPs shift to lower energy, which is consistent with the reduction of Rh. This trend is clearly seen in Fig. 1 for the peak positions of Rh $3d_{5/2}$ and Rh $3d_{3/2}$. For the Rh 3*d* peaks, their difference in BE varied from about 0.15 to 0.28 eV as alloy composition altered. With a given experimental resolution (refer to the Methods section), this can be treated as detectable (e.g. worth discussion) but not as a drastic difference. At the same time, the Cu $2p_{3/2}$ BEs of the bimetallic alloy NPs are shifted to higher energies, indicating the partial oxidation of Cu. We should note that the presence of partly oxidised Cu is beneficial for the catalyst; namely, in CO conversion. This also explains the slight improvement of CO conversion data for Rh_xCu_y alloy compared with that for monometallic Rh NPs, as can be seen in Figure SI 2(c). Once oxygen atoms are present on the surface of NPs, CO can react with O and desorb as CO_2. The synthesis conditions of Rh_xCu_y NPs and use of PVP, with chemically active oxygen and nitrogen, will tolerate partial oxidation of metals ions. For bimetallic Rh_xCu_y alloys, formation of complex Cu oxides inevitably affects the adsorption of ligands on Rh atoms, preventing oxidation of the latter. This trend is most prominent for Rh_xCu_y alloy NPs with comparable x:y ratio. In other words, Cu acts as a sacrificial anode to avoid the oxidation of Rh. Because all the NPs are capped with PVP, we assumed that the influence of this protective agent on the electronic structure of the NPs was the same in all cases, which is confirmed by the similar CL N 1*s* signal detected for all the NP samples (refer to Supplementary Figure SI 3). Therefore, we conclude that the changes observed in Rh 3*d* and Cu $2p_{3/2}$ CL HAXPES data originated from changes in the electronic structure of the NPs as a function of compositional alteration (different x:y ratios).

Previously reported size-dependent changes in the catalytic activity of Rh NPs indicate that smaller Rh NPs are more catalytically active than larger ones. We should stress that a difference in size of more than few nm is considered to be important for size-dependent studies. Such size-dependent changes in activity are attributed to changes in the ratio of rhodium surface oxide with a non-integer oxidation state ($Rh^{(3-\delta)+}$) to metallic Rh with NP size. For smaller NPs, a higher ratio of ($Rh^{(3-\delta)+}$) oxide leads to increased catalytic activity[32]. For example, Grass *et al.*[24] proposed a scenario in which the presence of an interface between the metallic core and surface metal oxide layer induces strain in the oxide, making it less stable and thus more reactive.

Formation of surface oxide is clearly seen in the Rh 3*d* HAXPES data acquired for monometallic Rh NPs (Fig. 1). The position of the Rh $3d_{5/2}$ peak for the Rh NPs indicates the coexistence of metallic Rh^0 and Rh oxide

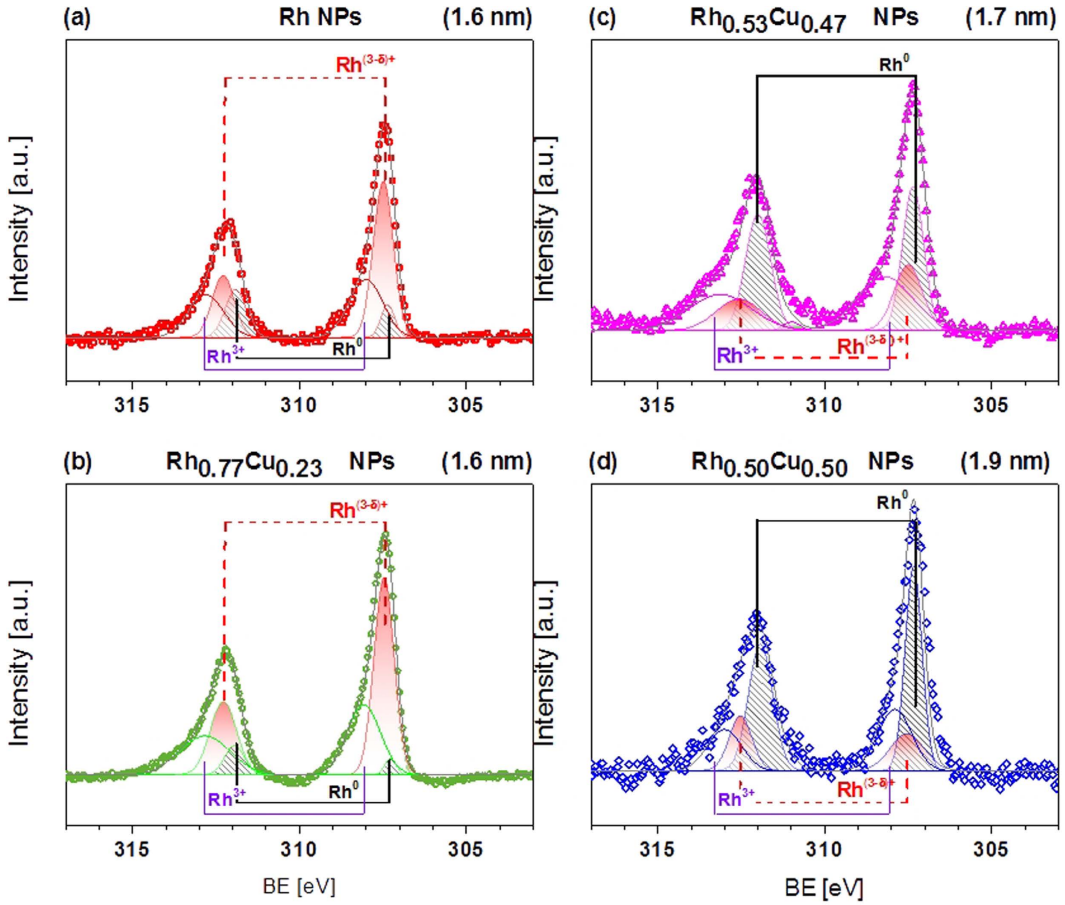

Figure 3. Fitting results of Rh 3*d* CL HAXPES data for (**a**) monometallic Rh NPs, (**b**) Rh-rich $Rh_{0.77}Cu_{0.23}$, (**c**) $Rh_{0.53}Cu_{0.47}$ and (**d**) $Rh_{0.50}Cu_{0.50}$ alloy NPs. Shaded areas are fitting results for metallic Rh^0 (black) and rhodium oxide with non-integer state $Rh^{(3-\delta)+}$ (red).

with a non-integer state $Rh^{(3-\delta)+}$. Formation of complex Rh NPs that contain metallic Rh^0 and Rh oxide with a non-integer state is favourable because it enhances CO oxidation, whereas a fully oxidised Rh_2O_3 surface layer will poison the reaction[33–35]. For this reason, we conclude that the catalytic activity observed for the monometallic Rh NPs, which is comparable to that of bulk Rh, originates from a surface Rh oxide layer with a non-integer oxidation state $Rh^{(3-\delta)+}$.

As mentioned above, for bimetallic Rh_xCu_y NPs with comparable x:y ratio, changes in electronic structure can be understood as simultaneous reduction of Rh and oxidation of Cu, implying that intermetallic charge transfer occurs from Cu to Rh (see the black solid lines used to mark the positions of Rh 3*d* and Cu $2p_{3/2}$ peaks in Figs 1 and 2). This statement is in agreement with the fitting results of Rh 3*d* CL HAXPES data shown in Fig. 3. The fitting results of CL HAXPES data indicate that the high catalytic activity of Rh-rich NPs (monometallic Rh and $Rh_{0.77}Cu_{0.23}$ NPs) originates from their relatively high ratio of reactive $Rh^{(3-\delta)+}$ oxide to metallic Rh formed during their solid solution synthesis, in agreement with previously reported data[34]. Remarkably, intermetallic interactions are even more important for bimetallic alloy NPs with comparable x:y ratio; e.g., $Rh_{0.53}Cu_{0.47}$ and $Rh_{0.50}Cu_{0.50}$ NPs. For these samples, the fitting results of Rh 3*d* CL HAXPES data reveal a clear decrease in content of the reactive $Rh^{(3-\delta)+}$ oxide component (Fig. 3(c,d)). Based on the above reasoning, this should cause a noticeable decrease in the catalytic activity of $Rh_{0.53}Cu_{0.47}$ and $Rh_{0.50}Cu_{0.50}$ compared with that of monometallic Rh and $Rh_{0.77}Cu_{0.23}$ NPs, which is not the case. Although the content of the reactive $Rh^{(3-\delta)+}$ component decreases, Cu^{2+} simultaneously emerges in $Rh_{0.50}Cu_{0.50}$ and $Rh_{0.53}Cu_{0.47}$ alloy NPs (refer to the Cu 2*p* fitting results shown in the Supplementary Figure SI 5 (d) and (c), respectively). Previous studies report promotion of NOx reduction with CO of Cu-based catalysts supported on γ-Al_2O_3[36–38]. For example, Amano *et al.*[36] stated that the catalytic reduction of NO with CO was promoted by the redox behaviour of Cu^{2+}/Cu^{1+}; at the same time, catalytic oxidation of CO with O_2 was promoted by the redox cycle between Cu^{2+} and Cu^0 species at temperatures above 300 °C. The temperature-dependent catalytic activity data presented in Supplementary Figure SI 2 indicate that for Rh_xCu_y alloy NPs conversion of NOx and CO are dominant reactions because they occur at lower temperatures (around 200 °C) than hydrocarbon conversion (around 260 °C). We argue that intermetallic charge transfer helps to compensate for the decreased fraction of catalytically active $Rh^{(3-\delta)+}$ in $Rh_{0.53}Cu_{0.47}$ and $Rh_{0.50}Cu_{0.50}$, thus resulting in negligible change in the catalytic activities of these samples compared with that of Rh-rich NPs.

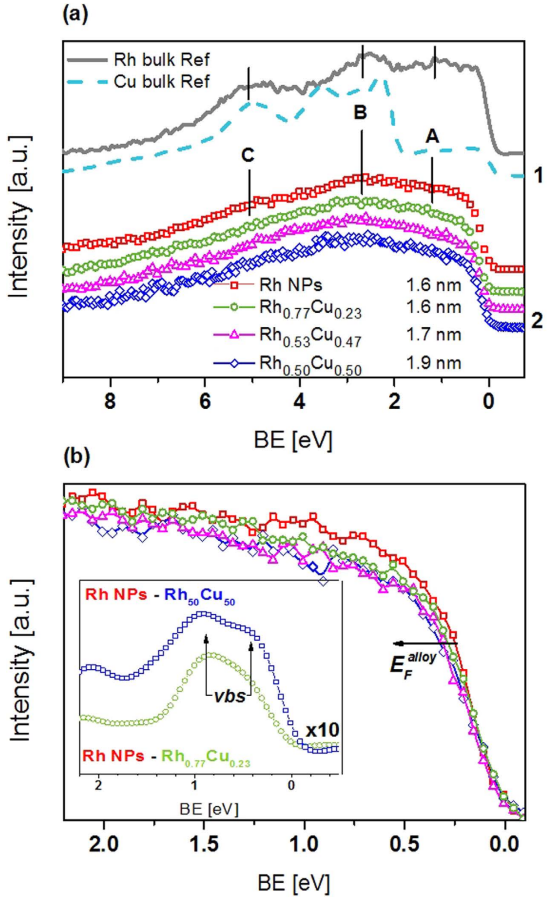

Figure 4. (**a**) VB HAXPES and (**b**) region near Fermi edge of $Rh_{0.77}Cu_{0.23}$, $Rh_{0.53}Cu_{0.47}$ and $Rh_{0.50}Cu_{0.50}$ alloy NPs. Rh and Cu bulk reference are shown in (**a**) section 1. The triplet structure characteristic for metallic Rh is labeled as peaks A-C. The energies of triplet structure are consisted with previously reported experimental data[41] and theoretical calculations[51]. Inset in (**b**) is the magnified differential spectra in the VB region near the Fermi edge. Maximum of differential spectra is located around 1 eV below Fermi level and associated with formation of Rh 4*d* and/or Rh-Cu virtual bound states (*vbs*) as a result of orbital hybridization caused by alloying. The position of (*vbs*) agreed well with data reported earlier for CuRh alloy[8].

From the discussion above, it becomes evident that Rh_xCu_y alloys with different compositions can be roughly divided into three groups: (i) Rh-rich, represented by monometallic Rh and $Rh_{0.77}Cu_{0.23}$ NPs, (ii) alloys with comparable x:y ratio like $Rh_{0.50}Cu_{0.50}$ and $Rh_{0.53}Cu_{0.47}$ NPs and (iii) Cu-rich NPs, which are not considered here because of challenges related with stabilisation of the nanoscale Cu^0 phase during synthesis. In this regard, the inclusion of an additional samples into our discussion, for example, NPs with $x \geq 0.6$, will presumably strengthen our current line of reasoning but will not provide much qualitatively new information because those NPs will fall into category (i); e.g. Rh-rich alloys.

VB HAXPES. The comparable CO-oxidising catalytic activity obtained for the samples intuitively implies that there is no drastic change in the electronic structure of the NP alloys as a function of the x:y ratio. This behaviour was confirmed by VB HAXPES measurements, as shown in Fig. 4(a). To allow comparison, all data were collected during the same beam time and the energy range of recorded VB was kept identical. Tougaard background was subtracted and the integrated area was used for signal normalisation. Additionally, section (1) of Fig. 4(a) shows the reference VB spectra of bulk Rh and Cu. Note that even though the VB spectra of the studied NPs lack pronounced fine structure, this is not because of the low experimental resolution of HAXPES measurements, but rather originates from the extremely small size of the NPs. The VB spectrum of bulk Rh acquired under similar experimental conditions supports this statement; it contains a well-resolved triplet structure characteristic of metallic Rh, as indicated by peak A-C in Fig. 4(a). For all NPs, the main contribution to the total DOS in the VB region is from degenerated Rh 4*d* states (cumulative effect of t_{2g} and e_g states[39]), because the photoionization cross-section of Rh 4*d* at 6 keV is approximately 6 times that for Cu 3*d*[40]. The energies of Rh 4*d* triplet structure A-C are consistent with previously reported experimental data as well as theoretical calculations[41–44]. In addition, reported VB data for larger monometallic Rh NPs (12.2 ± 1.6 nm) prepared in a similar manner qualitatively resemble the VB spectrum of bulk Rh[41].

For monometallic Rh NPs, triplet structure A-C is resolved, although its respective intensities are less pronounced than those of bulk Rh. The Fermi edge (E_F) of the NPs shifted to a higher energy compared with that

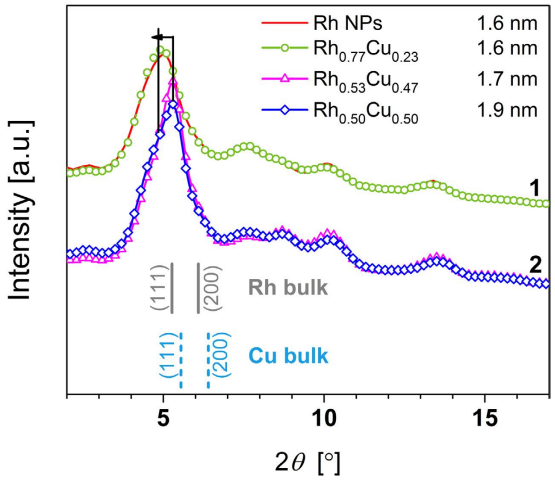

Figure 5. HEXRD pattern of monometallic Rh NPs, $Rh_{0.77}Cu_{0.23}$, $Rh_{0.53}Cu_{0.47}$ and $Rh_{0.50}Cu_{0.50}$ alloy NPs. The position of the first peak of monometallic Rh and Rh-rich NPs is shifted towards lower angle compared with that of alloy NPs with comparable x:y ratio, indicating higher oxide to metal content.

of bulk Rh. These differences are attributed to the cumulative effects of (i) extremely small particle size[45], (ii) narrowing of the d-band as a result of alloying (decreased overlap of the d-orbitals when the neighboring position around a given metal atom is occupied by another component of the alloy) and (iii) the influence of the surface layer (insulating PVP), which cannot be neglected for such small NPs. No VB HAXPES data for alloy NPs with extremely small particle size, such as those in this study, have been reported previously. The VB spectra of alloy NPs displayed in section (2) of Fig. 4(a) are qualitatively similar. Nevertheless, noticeable differences are observed upon comparing the VB HAXPES data for Rh-rich NPs and alloy NPs with comparable Rh:Cu ratio. While all other spectral features are very similar, the VB spectrum of the Rh-rich NPs is more intense in the BE range from 0.25 to 2.2 eV than that of the alloy NPs with comparable Rh:Cu ratio. This region of the VB spectra is worth studying in detail because the electronic structure near E_F affects catalytic activity. To emphasise observed differences in the VB spectra near E_F, magnified differential spectra are provided in the inset of Fig. 4(b).

For the alloy NPs, the lowering of DOS near E_F indicates that the alloy NPs are electron deficient relative to the bulk (supported by the CL fit). A possible explanation for this may be the formation of a virtual bound state (*vbs*) associated with Rh 4*d* and/or Rh-Cu bonds as a result of orbital hybridisation caused by alloying. The theory of a virtual bound state was first introduced by Friedel[46] and Anderson[47], and is also known as a model that describes the importance of *s-d* exchange (compensating of missing *d* charge with *s* charge) in alloys. Later, Seib and Spicer[48] proved this theory for CuNi and Ishii *et al.*[8] applied it to CuRh alloys. The latter researches estimated that the position of the virtual bound state was about 1.25 eV below E_F. This is consistent with data shown in the inset of Fig. 4(b) for $Rh_{0.50}Cu_{0.50}$ and $Rh_{0.77}Cu_{0.23}$ NPs, refer to the guide line marked as (*vbs*). Orbital hybridisation does not exclude the intermetallic charge transfer from Cu to Rh proposed above. On the contrary, hybridisation of Rh 4*d* and Cu 3*d* orbitals should manifest itself as the formation of bonding and antibonding states near E_F based on general understanding. However, this is not evident from the direct comparison of VB spectra because no additional features are clearly resolved. We should point out that determination of intermetallic charge transfer in metal alloys based solely on VB data is a difficult task, because even electron density calculations cannot precisely define the region of valence charge associated with each atom. However, comparison of VB and linear combination fitting data based on the reference bulk metals strengthens our argument by taking into account that the observed discrepancy is most pronounced at energies near E_F (refer to Supplementary Figure SI 7(b) and (d)). Additionally, the E_F shift for an alloy can be calculated by: $E_F^{alloy}(x) = xE_F^{Rh} + (1 - x)E_F^{Cu}$, where x is the concentration of parent Rh, and E_F^{Rh} (4.65 eV), E_F^{Cu} (4.47 eV) and E_F^{alloy}, are the Fermi levels of pure Rh, Cu and the alloy, respectively. This equation predicts a progressive shift to higher BE with increasing Cu content, which is consistent with the experimental data presented in Fig. 4(b) (refer to arrow labeled as E_F^{alloy}). At the same time, the asymmetry of the Cu $2p_{3/2}$ CL peak is small for all NPs, and the asymmetry of Rh 3*d* peaks is smaller for monometallic Rh and Rh-rich alloy NPs than those with a higher Cu content, implying that electron density is lowered at the Cu d-band; in other words, supporting the proposed scenario of intermetallic charge transfer from Cu to Rh. This reasoning is consistent with the findings reported for a $Pd_{0.50}Cu_{0.50}$ alloy system[49,50].

High-energy X-ray diffraction (HEXRD) data, as shown in Fig. 5, confirmed that the investigated samples can be divided into two groups; namely, Rh-rich NPs (section 1 of Fig. 5) and alloy NPs with comparable x:y ratio (section 2 of Fig. 5). Changes observed for the shape and position of the first peak (low 2θ) are consistent with conclusions drawn from CL and VB HAXPES data analysis. As described above, the electronic structure of the Rh-rich NPs is dominated by the formation of Rh oxide with a non-integer valence state. Generally, the d spacing of metal oxides is larger than that of the bulk metal. In angular-dependent XRD patterns, this should manifest as a shift of the main peak to lower 2θ value. This trend is clearly observed for the Rh-rich alloy NPs (section 1 of Fig. 5). For the alloy NPs with a higher fraction of metallic Rh, shape and position of the first peak exhibit

patterns with increased intensity of the Rh 111 peak at higher (2θ) values (section 2 of Fig. 5) compared with that for monometallic and Rh-rich NPs.

Conclusions

In conclusion, the change in electronic structure of extremely small Rh_xCu_y alloy NPs with different x:y ratios was investigated by CL and VB HAXPES, confirming that the electronic structure of these NPs is a function of their composition. For monometallic Rh and Rh-rich alloy NPs, formation of Rh surface oxide with a non-integer oxidation state ($Rh^{(3-\delta)+}$) is the main factor that leads to their high catalytic activity. Conversely, for alloy NPs with comparable x:y ratio ($Rh_{0.53}Cu_{0.47}$ and $Rh_{0.50}Cu_{0.50}$), the decreased fraction of catalytically active $Rh^{(3-\delta)+}$ oxide is compensated for by charge transfer from Cu to Rh, resulting in negligible change in their catalytic activities compared with those of Rh-rich and monometallic Rh NPs.

Methods

Synthesis of Rh_xCu_y alloy NPs. Rh_xCu_y alloy NPs with a narrow size distribution and diameter of about 2 nm were prepared by chemical reduction using rhodium(III) acetate $Rh(AcO)_3$ and copper(II) chloride $CuCl_2$ as metal precursors, and poly(N-vinyl-2-pyrrolidone) (PVP) as a protective agent. The strong base potassium tert-butoxide $(CH_3)_3COK$ was added to control the pH of the ethylene glycol solution, which was used as a reducing agent and buffer medium. The fabrication details of the alloy NPs can be found elsewhere[51].

Characterisation and catalytic activity of Rh_xCu_y alloy NPs. TEM analyses revealed that within the standard deviation, the size of Rh_xCu_y alloy NPs was independent of the Cu and Rh content and remained the same (at about 2 nm) for all samples (refer to Supplementary Figure SI 1). The x:y ratio in the prepared alloy NPs was determined by energy-dispersive X-ray elemental analysis. To investigate their catalytic activity, Rh_xCu_y NPs supported on γ-Al_2O_3 catalysts were prepared by wet impregnation. Details of the wet impregnation process can be found elsewhere[51]. The Rh_xCu_y NPs with different compositions exhibited comparable catalytic activity (Supplementary Figure SI 2).

Hard X-ray photoelectron spectroscopy (HAXPES). HAXPES CL and VB spectra for samples were recorded at the National Institute for Materials Science (NIMS) contract undulator beamline BL15XU at SPring-8, Japan[52,53]. A linearly polarised X-ray beam with an incident photon energy of 5.95 keV was used for HAXPES measurements. Use of hard X-rays enabled bulk-sensitive measurements to be performed. A high-resolution hemispherical analyser (VG Scienta R4000) was used to collect spectra. All data were recorded at room temperature with the take-off angle of photoelectrons with respect to the sample holder surface set to 88°. For an incident photon energy of 5.95 keV, the total energy resolution estimated using an Au reference sample was 240 meV. A combination of Tougaard and linear backgrounds was subtracted from the spectra and BEs were calibrated with respect to the Fermi edge of the Au reference. The effective information depth was approximately 17–20 nm, which was estimated using the equation proposed by Tanuma, Powell, and Penn (TPP-2M)[54]. This depth is an order of magnitude greater than the largest Rh_xCu_y NPs, indicating that the data provided a reliable account of the electronic structure of the NPs.

High energy X-ray diffraction (HEXRD) experiments. HEXRD data were obtained by two-axis diffractometer installed at the beamline BL04B2 at SPring-8, Japan. The incident synchrotron X-ray of 61.37 keV was generated using an Si(111) monochromator. The accessible Q range was found to be 0.2 to 25 $Å^{-1}$ by measuring the scattering angle range from 0.3 to 48.9° at intervals of 0.1° with an exposure time of 20 s using three CdTe detectors. The HEXRD measurements for all NP samples were performed in symmetric transmission geometry at room temperature.

References

1. Balaj, O., Balteanu, I., Rossteuscher, T. & Beyer, M. Bondybey, Catalytic oxidation of CO with N_2O gas-phase platimun clusters. *Angew. Chem., Int. Ed.* **43,** 6519 (2004).
2. Zhang, H., Jin, M. & Xia, Y. Enhancing the catalytic and electrocatalytic properties of Pt-based catalysts by forming bimetallic nanocrystals with Pd. *Chem. Soc. Rev.* **41,** 8035–8049 (2012).
3. Habas, S. E., Lee, H., Radmilovic, V., Somorjai, G. A. & Yang, P. Shaping binary metal nanocrystals through epitaxial seeded growth. *Nat. Mater.* **6,** 692 (2007).
4. Hyman, M. P., Loveless, B. T. & Medlin, J. W. A density functional theory study of H_2S decomposition on the (111) surfaces of model Pd-alloys. *Surf. Sci.* **601,** 5382–5393 (2007).
5. Shao, M., Liu, P., Zhang, J. & Adzic, R. Origin of enhanced activity in palladium alloy electrocatalysts for oxygen reduction reaction. *J. Phys. Chem. B* **111,** 6772–6775 (2007).
6. Hammer, B. & Nørskov, J. K. Electronic factors determining the reactivity of metal surfaces. *Surf. Sci.* **343,** 211–220 (1995).
7. Hammer, B. & Nørskov, J. K. Theoretical surface science and catalysis-calculations and concepts. *Adv. catal.* **45,** 71–129 (2000).
8. Ishii, H., Miyahara, T., Hanyu, T. & Yamaguchi, S. Photoelectron spectra of pure Rh metal and CuRh alloys. *J. Phys. Soc. Jpn.* **53,** 2151–2156 (1984).
9. Ebert, H., Winter, H., Abart, J. & Voitlander, J. Magnetic and electronic properties of the alloy system Cu*x*Rh_{1-x}. *J. Phys. F.* **17,** 1457–1469 (1987).
10. Ponec, V. & Bond, G. C. *Catalysis by metals and alloys.* **95** (Elsevier, 1995).
11. Spivey, J., Han, Y. F. & Dooley, K. M. eds. *Catalysis, A review of recent literature* **28,** (Specialist periodical Reports, Royal Society of Chemistry, 2016).
12. Fritz, A. & Pitchon, V. The current state of research on automotive lean NO_x catalysis. *Appl. Catal., B.* **13,** 1–25 (1997).
13. Roy, S., Hegde, M. S. & Madras, G. Catalysis for NOx abatement. *Appl. Energy* **86,** 2283–2297 (2009).
14. Kim, S. *et al.* Trend of catalytic activity of CO oxidation on Rh and Ru nanoparticles: role of surface oxide. *Catal. Today* **185,** 131–137 (2012).
15. Chorkendorff, I. & Niemantsverdriet, J. W. *Concepts of modern catalysis and kinetics* (John Wiley & Sons, 2006).
16. Twigg, M. V. Progress and future challenges in controlling automotive exhaust gas emissions. *Appl. Catal., B.* **70,** 2–15 (2007).

17. Twigg, M. V. Catalytic control of emissions from cars. *Catal. Today* **163,** 33–41 (2011).
18. Meguerian, G. H., Hirschberg, E. H. & Rakowsky, F. W. *U.S. Patent No. 4,006,103*, U.S. Patent and Trademark Office (1977).
19. Krummenacher, J. J., West, K. N. & Schmidt, L. D. Catalytic partial oxidation of higher hydrocarbons at millisecond contact times: decane, hexadecane, and diesel fuel. *J. Catal.* **215,** 332–343 (2003).
20. Shelef, M. & Graham, G. W. Why rhodium in automotive three-way catalysts? *Cat. Rev. - Sci. Eng.* **36,** 433–457 (1994).
21. Zhdanov, V. P. & Kasemo, B. Mechanism and kinetics of the NO-CO reaction on Rh. *Surf. Sci. Rep.* **29,** 31–90 (1997).
22. Joyner, R. W. & van Santen, R. A. eds *Elementary Reaction Steps in Heterogeneous Catalysis* **398,** (Springer Science and Business Media) (2012).
23. Abe, Y., Kato, K., Kawamura, M. & Sasaki, K. Rhodium and rhodium oxide thin films characterized by XPS. *Surf. Sci. Spectra* **8,** 117–125 (2001).
24. Grass, M. E. *et al.* A reactive oxide overlayer on Rhodium nanoparticles during CO oxidation and its size dependence studied by *in situ* Ambient Pressure X-ray Photoelectron Spectroscopy. *Angew. Chem. Int. Ed.* **47,** 8893–8896 (2008).
25. Lundgren, E. *et al.* Surface oxides on close-packed surfaces of late transition metals. *J. Phys.: Condens. Matter* **18,** R481 (2006).
26. Blomberg, S. *et al.* A high pressure X-ray photoelectron spectroscopy study of oxidation and reduction of Rh (100) and Rh nanoparticles. *Surf. Sci.* **628,** 153–158 (2014).
27. Matsuo, P. J., Standaert, T. E. F. M., Allen, S. D., Oehrlein, G. S. & Dalton, T. J. Characterization of Al, Cu, and TiN surface cleaning following a low-K dielectric etch. *J. Vac. Sci. Technol.* **17,** 1435–1447 (1999).
28. Ghijsen, J. *et al.* Electronic structure of Cu_2O and CuO. *Phys. Rev. B* **38,** 11322 (1988).
29. Yin, M. *et al.* Copper oxide nanocrystals. *J. Am. Chem. Soc.* **127,** 9506–9511 (2005).
30. Miedema, A. R. The electronegativity parameter for transition metals: heat of formation and charge transfer in alloys. *J. Less-Common Met.* **32,** 117–136 (1973).
31. Lide, D. R. (Ed.). *CRC handbook of chemistry and physics* 85, Section 9, Molecular Structure and Spectroscopy; Electronegativity, CRC press (2004).
32. Vis, J. C., Van't B, H. F. J., Huizinga, T., Van Grondelle, J. & Prins, R. Reduction and oxidation of Rh/Al_2O_3 and Rh/TiO_2 catalysts as studied by temperature-programmed reduction and oxidation. *J. Mol. Catal.* **25,** 367–378 (1984).
33. Flege, J. I. & Sutter, P. *In situ* structural imaging of CO oxidation catalysis on oxidized Rh (111). *Phys. Rev. B* **78,** 153402 (2008).
34. Westerström, R. *et al.* Structure and reactivity of a model catalyst alloy under realistic conditions. *J. Phys.: Condens. Matter* **20,** 184018 (2008).
35. Peden, C. H. F. *et al.* Kinetics of carbon monoxide oxidation by oxygen or nitric oxide on rhodium (111) and rhodium (100) single crystals. *J. Phys. Chem.* **92,** 1563–1567 (1988).
36. Amano, F., Suzuki, S., Yamamoto, T. & Tanaka, T. One-electron reducibility of isolated copper oxide on alumina for selective NO-CO reaction. *Appl. Catal., B* **64,** 282–289 (2006).
37. Kacimi, M., Ziyad, M. & Liotta, L. F. Cu on amorphous AlPO4: Preparation, characterization and catalytic activity in NO reduction by CO in presence of oxygen. *Catal. Today* **241,** 151–158 (2015).
38. Hu, Y. *et al.* Influence of supports on the activities of copper oxide species in the low-temperature NO+ CO reaction. *Appl. Catal., B* **31,** 61–69 (2001).
39. Papaconstantopoulos, D. A. *Handbook of the band structure of elemental solids* (New York. Plenum Press, (1986).
40. Veigele, W. J. Photon cross sections from 0.1 keV to 1 MeV for elements Z = 1 to Z = 94. *Atomic Data and Nuclear Data Tables* **5,** 51–111 (1973).
41. Yang, A. *et al.* The valence band structure of Ag_xRh_{1-x} alloy nanoparticles. *Appl. Phys. Lett.* **105,** 153109 (2014).
42. Smith, N. V., Wertheim, G. K., Hüfner, S. & Traum, M. Photoemission spectra and band structures of d-band metals. IV. X-ray photoemission spectra and densities of states in Rh, Pd, Ag, Ir, Pt, and Au. *Phys. Rev. B* **10,** 3197 (1974).
43. Höchst, H. & Kelly, M. K. Resonant valence-band photoemission from rhodium. *Phys. Rev. B* **30,** 1708 (1984).
44. Tripathi, G. S., Brener, N. E. & Callaway, J. Electronic structure of rhodium. *Phys. Rev. B* **38,** 10454 (1988).
45. Höfelmeyer, J. D., Liu, H., Somorjai, G. A. & Tilley, T. D. Reverse micelle synthesis of rhodium nanoparticles. *J. Colloid Interface Sci.* **309,** 86–93 (2007).
46. Friedel, J. Sur la structure électronique des métaux et alliages de transition et des métaux lourds. *J. Phys. Radium* **19,** 573–581 (1958).
47. Anderson, P. W. Localized magnetic states in metals. *Phys. Rev.* **124,** 41 (1961).
48. Seib, D. H. & Spicer, W. E. Photoemission and Optical Studies of Cu-Ni Alloys. I. Cu-Rich Alloys. *Phys. Rev. B* **2,** 1676–1693 (1970).
49. Faulkner, J. S. & Jordan, R. G. *Metallic alloys: experimental and theoretical perspectives* (Springer Science & Business Media, 2012).
50. Weightman, P., Cole, R. J., Brooks, N. J. & Thornton, J. M. C. A new approach to the determination of charge transfer in metal alloys. *Nucl. Instrum. Methods Phys. Res. B* **97,** 472–478 (1995).
51. Komatsu, T. *et al.* First-Principles Calculation, Synthesis and Catalytic Properties of Rh-Cu Alloy Nanoparticles *Chem. Eur. J.* **23,** 57–60 (2017).
52. Ueda, S. Application of hard X-ray photoelectron spectroscopy to electronic structure measurements for various functional materials. *J. Electron. Spectrosc. Relat. Phenom.* **190,** 235–241 (2013).
53. Ueda, S. *et al.* Present status of the NIMS contract beamline BL15XU at SPring-8. *AIP Conf. Proc.* **1234**, 403 (2010).
54. Tanuma, S., Powell, C. J. & Penn, D. R. Calculations of electron inelastic mean free paths for 31 materials. *Surf. Interface Anal.* **11,** 577 (1988).

Acknowledgements

The authors would like to express theirs gratitude to Dr. Shigenori Ueda for support, helpful discussions and insights. This work was supported by ACCEL, Japan Science and Technology (JST). HAXPES measurements were performed with the approval of NIMS at the NIMS Synchrotron X-ray Station at SPring-8 under proposals No. 2015B4907 and No. 2016A4904 as part of the NIMS Nanotechnology Platform (Project No A-15-NM-0138 and No A-16-NM-0005) on microstructural characterisation. HEXRD measurements were carried out at SPring-8 with the approval of the Japan Synchrotron Radiation Research Institute (JASRI) under proposal No. 2015B1245 and No. 2016A1292. This work was also partly supported by the Ministry of Education, Culture, Sports, Science and Technology of Japan (OS: 15K04616). The authors are grateful to HiSOR, Hiroshima University and JAEA/SPring-8 for the development of HAXPES at the BL15XU beam line of SPring-8.

Author Contributions

H. Kitagawa and O.S. planned and supervised the project. H. Kitagawa, H.K., and K.K. designed the concept of NPs synthesis, T.K. synthesized NPs and performed initial characterization. K.S. and K.N. performed catalytic activity measurements. O.S. and H. Kitagawa designed X-ray based experiments, N.P., L.S.R.K., C.S. and O.S. conducted X-ray based characterization, N.P. analysed the X-ray based data. N.P. and O.S. wrote the manuscript with contributions from all co-authors.

Additional Information

Supplementary information accompanies this paper at http://www.nature.com/srep

Competing financial interests: The authors declare no competing financial interests.

How to cite this article: Palina, N. *et al.* Electronic Structure Evolution with Composition Alteration of Rh_xCu_y Alloy Nanoparticles. *Sci. Rep.* **7**, 41264; doi: 10.1038/srep41264 (2017).

Publisher's note: Springer Nature remains neutral with regard to jurisdictional claims in published maps and institutional affiliations.